

Petrology and paleokarst features of the Gomba hydrocarbon reservoir (central Hungary)

Márton Bauer*, Tivadar M. Tóth, Béla Raucsik, István Garaguly

Department of Mineralogy, Geochemistry and Petrology, University of Szeged, Szeged, Hungary

Received: February 15, 2016; accepted: July 26, 2016

The pre-Cenozoic basement of central Hungary is partly made up of different types of carbonate rocks. These carbonates are often good hydrocarbon reservoirs, and hydrocarbon production is significant in this region in Hungary. Nonetheless, the petrography of the reservoir rocks has not yet been investigated in detail. In this study, the results of the investigations of the lithology of a carbonate hydrocarbon reservoir from central Hungary (Gomba Field) are presented. Based on this work, two types of pure limestone, a dolomitic limestone and a polymictic breccia, could be distinguished in the study area. The limestone types are similar to the Kisfennsík Limestone Member and the Berva Limestone of the Bükk Mountains, but they contain significant amounts of framboidal pyrite and dead oil as vein fillings. The breccia is predominantly composed of angular carbonate clasts and minor metamorphic and sedimentary rock fragments in a chaotic pattern. The breccia has some grains that may be speleothems (e.g., stalactite or stalagmite) based on their structure and isotopic compositions. The fabric of the breccia suggests that it may have been formed by fluid-related processes. Cross-cutting relationships of the veins and petrography of the vein fillings suggest that there are four different fracture generations and two different hydrocarbon migration phases to be distinguished. The composition of the hydrocarbon-bearing fluid inclusions related to the second migration event is similar to the crude oil currently produced from the Gomba Field. During the Eocene, the Triassic basement was buried and brecciated. Subsequently, a primary hydrocarbon migration can be assumed, but the hydrocarbons became overmature, apparently due to the high temperatures of the burial environment. Finally, an uplift phase began and the youngest fracture generation formed, which serves as a primary pathway for the more recent hydrocarbon migration.

Keywords: Gomba Field, breccia, regolith, paleokarst, Hungarian Paleogene Basin

*Corresponding author: Márton Bauer; Department of Mineralogy, Geochemistry and Petrology, University of Szeged, Egyetem utca 2–4, H-6723 Szeged, Hungary
E-mail: baumart87@gmail.com

This is an open-access article distributed under the terms of the Creative Commons Attribution License, which permits unrestricted use, distribution, and reproduction in any medium for non-commercial purposes, provided the original author and source are credited.

Introduction

More than 60% of the world's oil and 40% of its gas reserves are stored in fractured carbonate reservoirs. The pre-Cenozoic basement of Hungary has a significant volume of carbonate rocks, which locally are excellent reservoirs. There are six Total Petroleum Systems known in the Pannonian Basin Province (Kókai and Pogácsás 1991; Dolton 2006). One of the most complex and most important of these is the Paleogene Petroleum System, which is located in the Hungarian Paleogene Basin in the central part of Hungary (Fig. 1). The study area is the Gomba Field in the western part of the basin. The field has Triassic carbonate and Eocene–Oligocene detrital reservoir rocks, complex structural and sedimentary traps, and source rocks of supposedly Pliocene age. Hydrocarbon exploration and production from Gomba only began at the end of the 1990s (Dolton 2006), but today it is one of the most productive areas in the country.

Although the production history is not long, local geologic and geophysical research has a far reaching past. The structure of the region is well known from geophysical investigations, but the petrography of the Triassic reservoir is less known because of the few cores and the very restricted number of analyses. Nevertheless, the production history clearly shows that the available geologic and fractured reservoir models do not fit well enough to explain past production and predict future trends. Thus, it is essential to improve our understanding of the geology of the area.

Based on the available reports and unpublished information, the carbonate part of the reservoirs may have paleokarst features (e.g., paleocave facies, large caverns, or collapse structures), which can significantly modify the porosity and permeability of the reservoir. Karst processes may increase or decrease porosity, modify migration pathways through cave passages, or collapse structures, and thus significantly change the hydraulic behavior of the complex reservoir. Nevertheless, it is very problematic to localize the effect of karst processes in the subsurface even though there are numerous studies by several authors on understanding the hydrodynamic role of paleocaves, including Lucia (1968, 1995, 1996), Candelaria and Reed (1992), Lucia et al. (1992), Fritz et al. (1993), Loucks (1999), and Loucks et al. (2004). Based on these works, some typical paleocave formations are recognizable not only by well-log analysis but also in cores or thin sections.

Our goals are to observe, document, and interpret the petrographic features of the Triassic carbonate rocks and their microfracture network in the study area based on an analysis of the core material. The main aim is to recognize the evolutionary history of the Triassic beds from the early diagenetic processes to the present day, recognize the main hydrocarbon migration pathways and estimate the effects of the karst forms in the reservoir.

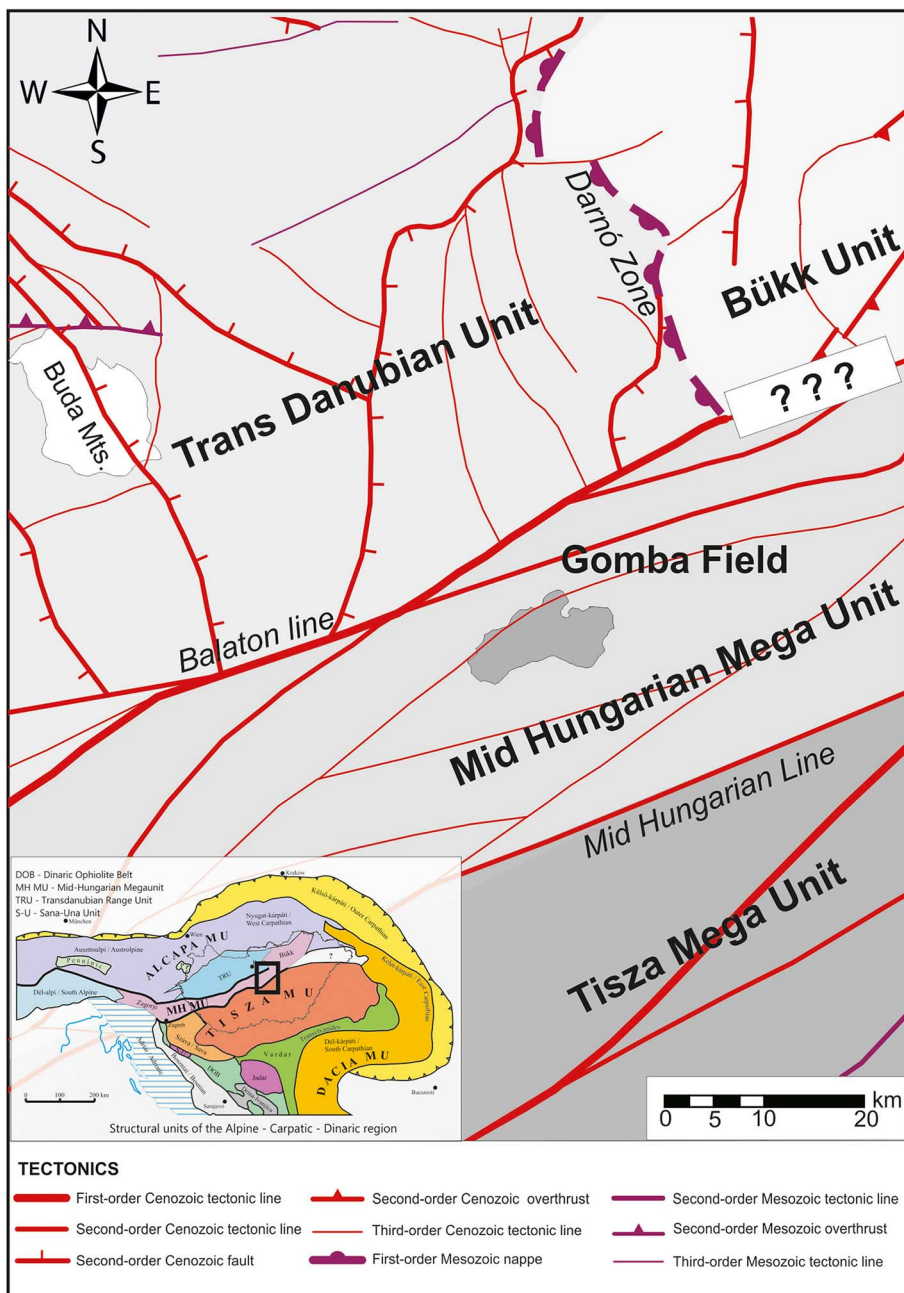


Fig. 1
Geologic setting of the investigated area (based on Haas et al. 2010)

Geologic setting

The investigated area is located in the northern part of mid Hungary and western part of the Hungarian Paleogene Basin, which was subdivided into three parts by Nagymarosy (1990). The Gomba Field belongs to the southern Buda Paleogene unit. According to the Pre-Cenozoic Basement Map of Haas et al. (2010), the region is located at the boundary of the Transdanubian Range Unit (TRU) and the Mid-Hungarian Unit (MHU) (Fig. 1). The boundary between the TRU and MHU is defined by the Balaton Line, a significant transversal fault zone, while the position of the boundary of the TRU and the Bükk Unit to the north is rather problematic. Though the boundary is unequivocally inferred by seismic studies (Szalay et al. 1976, 1978), supposed Bükk-type lithologies were also penetrated by deep wells on the opposite side of the hypothetical tectonic zone (Benedek 2009).

The Mesozoic sequence of the MHU is poorly known, but it greatly differs from the typical Mesozoic formations of both the TRU and the Bükk Unit. A close correlation with the Dinarides and the Southern Alps was suggested for the lithologies of the MHU (Haas 2004; Schmid et al. 2008). The relationship is discussed by numerous authors concerning both sedimentology and tectonic aspects (Árkai 1983; Kovács et al. 2000; Schmid et al. 2008).

While the Mesozoic rocks in the MHU are unknown at surface, the formations of both the TRU and the Bükk Unit have been studied in detail in outcrop. The closest outcrops in the TRU to the investigated reservoir are located in the Buda Mountains, where Ladinian dolomitized platform carbonates (Budaörs Dolomite Formation), Carnian–Norian platform dolomite and limestone (Dachstein Limestone Formation), and cherty basinal limestone (e.g., Mátyáshegy Formation) represent the Mesozoic sequence. The limestone and dolomite bodies in the Buda Mountains contain significant karst cavities and caves formed primarily by epigene (Wein 1977; Nádor and Sásdi 1991) and young, still active hypogene processes (Kriván 1959; Kraus 1982; Nádor 1991; Nádor and Sásdi 1995). Paleokarst features of Mesozoic–Tertiary carbonates of the Buda Hills were studied by Korpás and Juhász (1990), Esteban et al. (2009), Györi et al. (2011), and Poros et al. (2012).

As far as the Bükk Unit is concerned, the limestone-dominated sequences are recrystallized and generally reached anchimetamorphic grade (Árkai 1983) with the degree of metamorphism decreasing from NE to SW. According to the present-day lithostratigraphic concepts, the different Middle to Upper Triassic platform carbonates in the Bükk Unit are assigned to the Bükkfensík Limestone Formation (Haas 2004). A peculiar, non-metamorphosed variety of these almost pure carbonate rocks is restricted to the NE part of the Bükk Mountains, called the Kisfensík Limestone Member. The unit most likely forms a small thrust sheet (Haas 2004).

The Kisfensík Limestone consists of predominantly light-gray, whitish-yellow carbonate platform-facies limestone. Tidal flat, lagoonal, and reefal environments can be reconstructed in the carbonate platform sequence of the Kisfensík block. The sequence is mainly thick-bedded or massive, containing subordinate finely bedded

parts and occasionally cyclic loferites. Syngenetic brecciation is relatively frequent (Pelikán 2005). Although the type area of the formation is located in the NE part of the Bükk Mountains, there are some proven occurrences in the subsurface to the SW of that range. The Berva Limestone is found in the southern part of the Bükk Mountains. It has a very similar appearance to the Kisfennsík Limestone, but it contains much more fossil material. It is the typical formation at the southern margin of the Bükk Mountains (Less 2005). Early karstification of the Kisfennsík Limestone was proven by Velledits et al. (1999). Karstification of the Berva Limestone has not yet been investigated. Neither the Kisfennsík Limestone Member (North Bükk Mountains) nor the Berva Limestone (South Bükk Mountains) is metamorphosed (Less 2005).

The studied region is characterized by continuous sedimentation from the Eocene to the Miocene with numerous subsequent transgressive and regressive cycles (Benedek 2009). The Eocene strata everywhere overlie the strongly deformed Mesozoic structures with an angular unconformity and variable absence of sedimentation (Keckskeméti 1998; Less 2005). As a result, different marly and clayey sediments and carbonate rocks were formed. Siliciclastic sequences were also deposited during the Miocene (Tari et al. 1993) (Fig. 2).

One of the most important events concerning the reservoir’s evolution was the development of the Eocene-aged Basal Paleogene Clastics (BPC), the Kosd Formation (?), which consists predominantly of debris of gray claystone, sandstone, limestone, and dolomite gravel; occasionally, mollusk-bearing marl is present with fresh-water

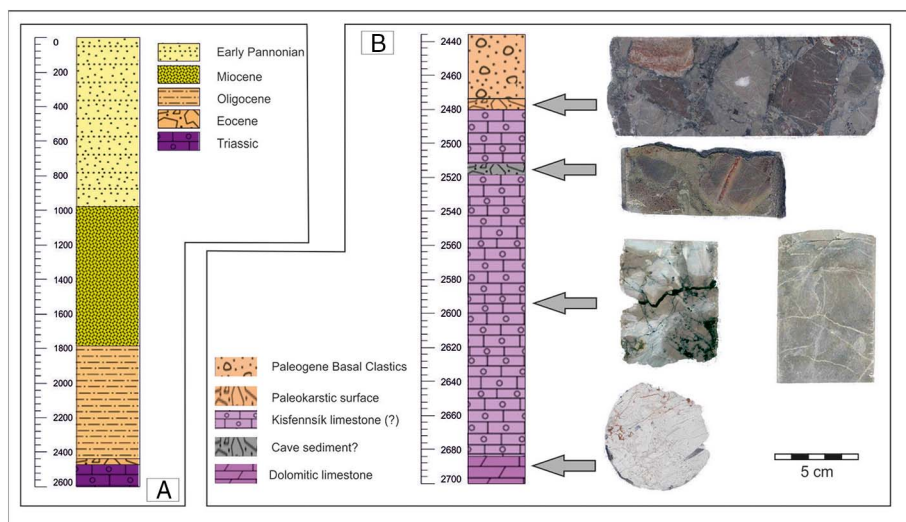


Fig. 2
 A: Idealized stratigraphy of the investigated wells. B: Detailed and idealized stratigraphy and the investigated cores

limestone and coal in the upper part of the sequence (Less 2005). The basal member of the formation contains 2–25-cm-large boulders and gravel, interpreted as erosional debris from the underlying Kisfennsík Limestone (Less 2005). During the Oligocene, fine-grained (hemi-) pelagic sediments were deposited, e.g., the Tard Clay Formation and the Kiscell Clay Formation. The former is characterized by high TOC content, having reached the oil window during the Pliocene (5 Ma); therefore, this formation is regarded as a source rock for HC generation, approximately 2,400 m below the present-day surface (Benedek 2009).

The reservoir rocks in this area are intensely tectonized. The basin's morphology is controlled by complex fault patterns of predominantly NE–SW strike that were essentially caused by numerous subsequent Eo-Alpine compression phases (Austrian, Pyrenean) and Neo-Alpine (Late Miocene) transversal faults (Csontos and Nagymarosy 1998; Fig. 1). The Neogene structural pattern of the basin is mainly the result of these transversal movements; some of the faults can be interpreted as rejuvenated old structures. This complicated fault pattern is assumed to have had a significant influence on the deep basinal hydrological actual and pale flow system of the reservoir.

Exploration of the Gomba Field began toward the end of the 1990s. Based on the petrographic investigation of cores and chips, the Triassic carbonate reservoir shows the characteristics of the Kisfennsík Limestone, so the area is interpreted as a part of the Bükk Unit. However, the stratigraphic classification is questionable; hence, the classification of formations in this study should also be considered restricted. Similar to the Kisfennsík Limestone Formation, the Berva Limestone is also a non-metamorphic formation, and its South Bükk range is closer to the examined area than the Kisfennsík Limestone. Moreover, the classification of the conglomerate covering the carbonate as the Kosd Formation is also debatable; thus, this section was named BPC. Upsection the Eocene debris, with high fluid storage capacity, is similar to the Kosd Formation.

Based on the present hydrodynamic model, the fractured Triassic carbonates and the Eocene debris behave as a continuous hydraulic system (Benedek 2009). The groundwater beneath the hydrocarbons has a temperature of ~120 °C with a salinity of ~35%. As a consequence, it seems possible that the rock body is still under the control of hypogenic karstification following the Cenozoic exhumation-related surficial karstification. Understanding the ongoing karstic processes is one of the most important steps in studying the hydrodynamic system of the reservoir.

Materials and methods

The occasional total mud loss at certain levels of all (seven) boreholes during the drilling process suggests intervals with significant open cavernous pores and extremely high permeability, which explains why a rather limited number of samples were able to be collected. Hence, the sampling strategy was to concentrate on core material

representing zones of the reservoir as close as possible to the highest porosity horizons. Following a careful macroscopic description, 5 × 5-cm-sized thin sections were made from the available cores. The analyzed material and the applied methods are summarized in Table 1.

Fabric

The rock fabric was observed under an Olympus SZX7 binocular microscope at thin section scale and was classified after Dunham (1962) for the limestone and after Sibley and Gregg's (1987) classification schemes for dolomite. Vein texture classification was made according to Bons et al. (2012). Petrographic Image Analysis (PIA) was used to characterize the breccia samples following Mort and Woodcock's (2008) scheme.

The input images were generated using thin sections in a 6,000 dpi resolution slide scanner. The Corel Draw X3, Olympus Stream Essential, ImageJ, and Fractalys software were used for image analysis and the following geometric parameters were measured.

Particle size distribution

There is a close relationship between the formation process and the clast size distribution of the breccia zones, which is why the particle-size distribution (PSD) is

Table 1

Summarized table of the measurements. Forty-two cores were examined altogether. On average they were 20 cm long so about 8 m of core were macroscopically examined. Thin sections are 30 µm thin

	Gomba-1 well	Gomba-3 well	Gomba-6 well
Macroscopic core description	12	26	4
Thin section analysis	9	17	4
Computer image analysis	3	17	4
Cathodoluminescence microscopy	–	3	–
UV microscopy	–	18	–
Scanning electron microscopy	–	2	–
Raman spectroscopy	–	18	–
Microthermometry	–	18	–
X-ray powder diffraction	–	5	8
X-ray fluorescence spectrometry	–	3	–
Stable isotope analysis	–	14	–

one of the most generally measured geometric parameters (Jébrak 1997). Numerous structural geological studies showed that PSD follows the

$$N(r) = C * r^B$$

power law distribution function at each scale, where $N(r)$ means the number of clasts greater than r in diameter, C is a constant, and B is the gradient of the linear function in logarithmic scale. The calculations were carried out using the squared area parameter in pixels according to Blenkinsop (1991).

Clast/matrix proportion

To calculate this parameter, the areas covered by clasts and matrix were considered first on the surface of the thin section. The proportion of the clasts and matrix was computed as the thin section area/total clast area.

Rotation

Grain orientation was characterized numerically by the variation coefficient of the main axes of the ellipses fitted to the clasts. The ellipse fitting method equates the second-order central moments of the ellipse to those of the distribution, thereby effectively defining both the shape and size of the ellipse.

Roundness

Roundness is a parameter that quantifies the shape of the clasts. It was calculated using the ImageJ software with the following function: $\text{Round} = 4 * [\text{Area}/\pi * \text{Major Axis}^2]$, where Major Axis concerns the fitted ellipse, which is fitted onto the individual clasts using the same method shown before.

Grain roughness

The fractal dilation method was used to analyze the roughness of the grains. It was originally developed by Flook (1978) and has been extensively used to measure the D (fractal dilation) of cellular borders. Dilation has several features that make it superior to other methods. The basic idea in the standard dilation method is that one takes convolution kernels of different sizes (diameters) and convolves them with the image border. Then, the resultant area is divided by the diameter of the kernel and the log of that result is plotted against the log of the kernel diameter. A fractal object gives a straight line with slope S and $D = 1 - S$.

The statistical database built from the above-mentioned parameters was analyzed by the SPSS 20 software. For extreme data handling, boxplots were used, and the Kolmogorov–Smirnov method was applied for the normality test of the parameters.

Phase analysis

The microtexture of the samples was analyzed with an Olympus BX41 polarization microscope. A cathodoluminescence (CL) microscope was used to characterize the overgrowth of the different constituents and cement minerals. CL microphotographs were taken at the Institute for Geological and Geochemical Research's Centre for Astronomy and Earth Sciences, Hungarian Academy of Sciences, using a Reliotron (cold cathode) instrument mounted on a Nikon Eclipse E600 microscope using a Nikon 4500 digital camera. The cathodoluminescent apparatus was operated at a 7–8 keV accelerating voltage and 0.25–0.63 mA beam current.

A Rigaku Ultima IV X-ray diffractometer was used to determine the mineralogical composition of the insoluble residue. Insoluble residue was prepared by digestion of the calcium carbonate by dissolution of bulk samples with 10 v/v% acetic acid at 20 °C. When choosing samples to dissolve, we took care that the samples would not be postdiagenetically fractured. To characterize the clay minerals, oriented specimens were measured on a fraction of <2 µm diameter. Air-dried and ethylene glycol-solvated (16 h, 60 °C) samples were X-rayed to identify the swelling clay species.

A U-RFL-T type UV fluorescence module and a UMNU2 type filter (exciting filter 420–480 nm, emission filter 520 IF, and dichromatic mirror 500 nm) were applied to detect the carbonaceous material in the thin section. This set was installed on an Olympus BX41 polarization microscope. Carbonaceous material analyses were performed on a Thermo Scientific DXR Raman microscope equipped with a diode-pumped frequency-doubled Nd-YAG laser at 10 mW maximum laser power. The samples were irradiated by laser light at a wavelength of 532.2 nm with the laser beam focused using a 100× objective lens, resulting in a spot size of ~0.7 µm. The backscattered light collected by the microscope objective was filtered via an edge filter, dispersed by a single grating (1,800 grooves mm⁻¹) and gathered in a CCD detector cooled to –20 °C by the Peltier effect. The instrument has a spectral resolution better than 2 cm⁻¹ and a spatial resolution of a few cubic micrometers; a 25 µm pinhole aperture was used for each measurement. In every case, 1 mW laser power was used to record the spectra. Sample exposures were obtained by operating the DXR Raman microscope in auto-exposure operating mode, in which the instrument attempts to reach a specified signal-to-noise (S/N) ratio during the measurement (in this case, S/N = 60).

We used UV methods to characterize the petroleum inclusions (from the vein system). During the detection, we used the above-mentioned Olympus microscope with an Olympus U-MNU-2 filter cube and an Olympus 100 W mercury light source. We collected 18 spectra during the measurement. To optimize the S/N ratios, we chose the spectrum of the highest intensity among the collected spectra of the single petroleum inclusions. To facilitate a comparison between different petroleum types, each spectrum was transformed into XYZ chromaticity coordinates and was plotted in the CIE-1931 chromaticity diagram (Smith and Guild 1931). This method was also applied to characterize the crude oil from the Gomba-1 well.

Mineral chemistry

The geochemical properties of the different rock-forming phases (including framework grains and cement) were analyzed by XRF and SEM EDS instruments. A Horiba Jobin Yvon XGT 500 microfluorescence spectrophotometer was used for the XRF measurements with a 15 keV accelerating voltage and 10 μm aperture size. Mg-content measurements of the calcites were recorded by a Hitachi S-4700 FE scanning electron microscope with an Energy Dispersive detector. All the measurements were made at a 20 keV acceleration voltage.

The carbon and oxygen isotopic compositions of selected textural elements were determined in the Institute for Geological and Geochemical Research, Hungarian Academy of Sciences using the following methods. Sampling was conducted using a hand-operated microdrill, and the recovered powder was put into a 10-ml threaded borosilicate bottle closed down by septum after the volume above carbonate was rinsed by He gas. Carbonate was exposed with water-free phosphoric acid (H_3PO_4) at a stable temperature (72 °C). After the 100% carbonate–acid reaction and after isotopic equilibrium was reached (2 h), the $\delta^{18}\text{O}$ and $\delta^{13}\text{C}$ values of the gas exposed from the carbonate were measured by a Finnigan delta plus XP vehicle carrier gas mass spectrometer (Spötl and Wennemann 2003). The institute applied the international standards NBS-18 and NBS-19 and Carrara lab standards. The results were related to the Vienna-PeeDee Belemnite (V-PDB) standard (Coplen 1996) and given in traditional $\delta^{18}\text{O}$ and $\delta^{13}\text{C}$ values (expressed in ‰) under the following formula: $\delta = (R_{\text{sample}}/R_{\text{standard}} - 1) \times 1,000$, where R_{sample} and R_{standard} are the $^{18}\text{O}/^{16}\text{O}$ and $^{13}\text{C}/^{12}\text{C}$ isotope ratios defined in the sample and the standard, respectively (McKinney et al. 1950). The uncertainty of the measurement was better than 0.2‰.

Thermometry

Due to the maturation of the organic matter (OM), significant irreversible modification can take place, which can be detected in Raman spectra. Numerous thermometry methods were calibrated for this phenomenon during recent decades (Yui et al. 1996; Beyssac et al. 2002; Rahl et al. 2005; Lahfid et al. 2010; Zhou et al. 2014). All the calibrated methods calculate the maximum temperature that the OM was subject to, considering the position of the graphitic peak and the amplitude, full-width at half-maximum (FWHM), and area of 3 or 4 defect peaks. From the above-mentioned thermometers, Beyssac et al. (2002), Rahl et al. (2005), and Lahfid et al.'s (2010) methods were used on 18 samples.

The Seasolve PeakFit 4.12 software program was employed to evaluate the Raman spectra. A Gaussian deconvolution approach based on the Voigt-type curve fitting procedure was used to determine the peak position (center), amplitude, FWHM, full-width at base, and integrated area of the bands of interest.

In our case, there is a possibility to determine the formation temperature of the vein filling phases by fluid-inclusion thermometry. Fluid-inclusion petrography and

microthermometry were performed on thin sections made from limestone samples. Prior to the analytical procedures, double-polished thick sections (75–150 μm) were prepared from the cores. The preparation of thick sections followed the instructions of Shepherd et al. (1985). The sections were then examined to classify fluid inclusion assemblages following the criteria of Goldstein and Reynolds (1994). Microthermometry was carried out using a Linkam THMSG-600 heating–freezing stage mounted on an Olympus BX-41 microscope. The stage was calibrated using synthetic fluid inclusions trapped in quartz. The homogenization temperatures (T_h) have standard errors of ± 1 °C. The homogenization temperature was usually determined by the cycling method (Goldstein and Reynolds 1994). The salinities of the aqueous inclusions were calculated from the final ice-melting temperatures [$T_m(\text{Ice})$] and reported in m/m% of NaCl equivalent (Bodnar 1993).

Results

The results show two different types of carbonates (limestone and dolomitic limestone); there is a thin polymictic breccia horizon in the upper part of each borehole (G1, G2, and G3) and there are breccia zones that are involved in the massive carbonate rock body. In the following section, the detailed results are given for each rock type separated.

Carbonates

The top of the pre-Cenozoic basement is marked by a sharp reflection in the seismic images, but due to the above-mentioned total mud loss, the Triassic/Eocene unconformity could not be detected precisely in the sampled core material. The boundary was defined only by well log parameters (porosity and total gamma). More precise petrophysical measurements are not available because there is no core from this depth.

Limestone

Below the unconformity, two limestone types can be defined at macroscopic scale: Type A is a light gray, massive oncoidal limestone, and Type B seems to be a leached variety of Type A with a light brown, whitish color, and hygroscopic behavior. The Type B limestone is very friable and weathered. Because it is known from only 40 cm thickness in one core from the bottom of the Gomba-1 well, it is interpreted as a stratigraphically irrelevant unit.

Limestone Type A

Texture and grain types. The Type A limestone is onco-bio-pel-sparite grainstone (Fig. 3A and B). It consists of peloids and oncoids with foraminifers, algae,

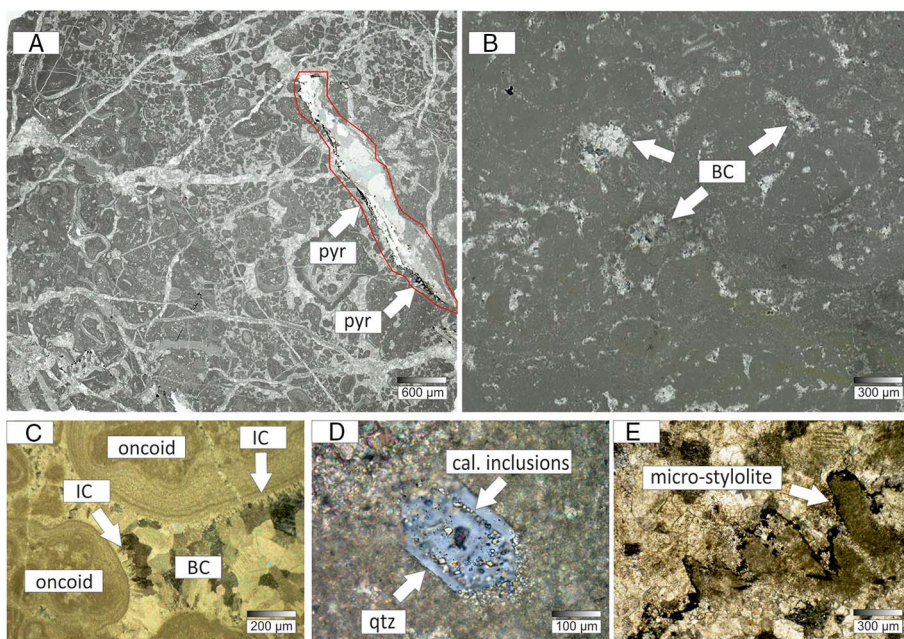


Fig. 3

A: Grainstone/packstone fabric of the limestone (Type A). The area included by the black line (in red online) probably the result of the sulfate reduction. B: Type B. C: Different cement types. D: Authigenic quartz with calcite inclusions. E: Microstylolite. (“A,” “B,” and “E” microphotos taken with planar light; “C” and “D” taken in polarized light)

echinoderms, and ostracod bioclasts in the center of the coated grains. The peloids and oncoïds are well sorted. The oncoïds are of 1–3 mm, and the peloids are of ~50 µm in diameter, of isometric shape. Coating-related laminae with microsparitic interlaminae infilling are well preserved. The grain-supported rock texture is observed to have several types of calcite spar filling the intergranular porosity. The samples contain (<1%) authigenic euhedral quartz crystals, which do not show fabric-selective distribution; rather, they are dispersed in the sediment (Fig. 3D). They always contain calcite inclusions.

Cement phases. The intraskeletal porosity is filled by microsparite, while the intergranular porosity is filled by an early isopach fibrous calcite cement and a later equigranular blocky calcite (BC) cement (Fig. 3C). Fenestral porosity is commonly filled by radiaxial fibrous calcite (RFC) cement, but micrite occurs as well. RFC and BC do not show luminescence, but the microsparite has a bright orange luminescent color.

Microstructure. Based on cross-cutting relationships and vein morphology, four fracture generations (F1, F2, F3, and F4) can be defined. The F1 generation can be characterized by syntaxial, symmetric BC veins (*sensu* Bons et al. 2012) (Fig. 4A).

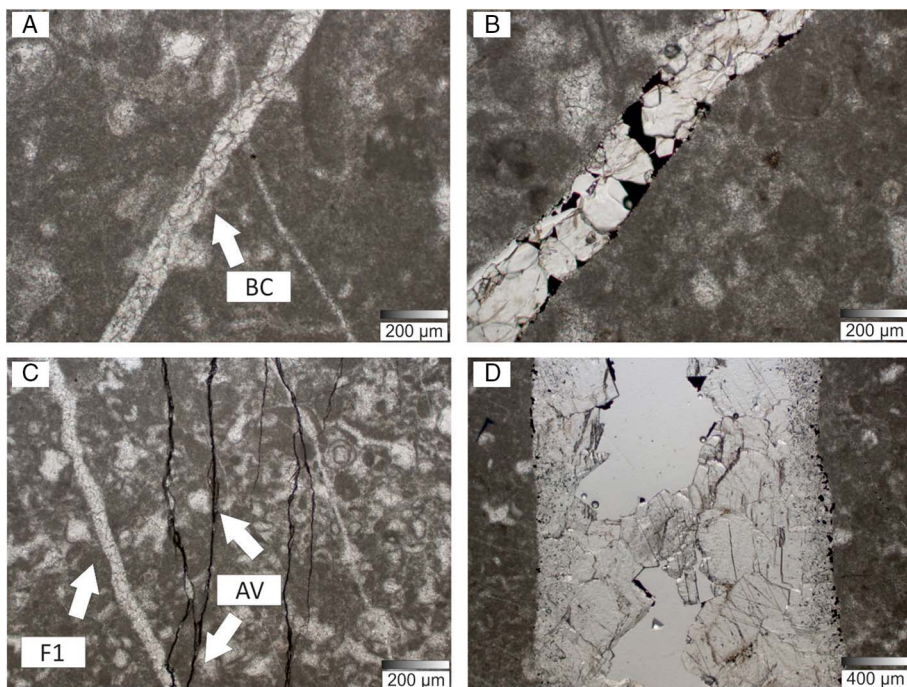


Fig. 4
Different vein types. A: F1 generation. B: F3 generation. C: F2 generation. D: F4 generation (All microphotos taken in planar light)

Feature indicative of growth competition are observable along both sides of the vein walls. The F1 vein generation seems to have been reactivated and encloses the F3 fracture generation. The F2 veins exhibit symmetric syntaxial vein morphology with elongated (150 µm long) calcite crystals (Fig. 4B). The distance of the opposite vein walls is approximately ~200 µm. Textural features of growth competition are not observed; nevertheless, a porosity increase related to dissolution is recognized. Both the primary intergranular and secondary pores are filled by bitumen. Raman spectroscopy measurements confirm the presence of organic material through its G (graphitic $-1,591\text{ cm}^{-1}$) and D1 (defect $-1,344\text{ cm}^{-1}$) bands. The F2-filling calcite crystals contain secondary oil fluid inclusions, which have a bright green color under UV light. Based on the CL images, the calcite cement growth was a multiphase process. The F3 generation is a narrow (<20 µm), dark-colored anastomosing vein type (Fig. 4C) with significant bitumen content. Microfabrics in this vein type are not detectable by petrographic tools because of the presence of the above-mentioned bitumen. Locally, the F3 fractures have much larger apertures and enclose ~40-µm-sized authigenic, bladed calcite crystals. The F4 vein generation has a

symmetric syntaxial vein morphology with an average diameter of >2 mm and consists of BC. Well-developed growth competition features are visible on the vein walls (Fig. 4D). The first calcite generation near the wall is bladed, but there are BC crystals along the inner side. All the calcite crystals are twinned. There is no intergranular porosity inside the veins, which are lined by micritic carbonate with abundant framboidal pyrite crystals.

The vein-filling calcite contains many primary and secondary water and oil inclusions. Water-containing fluid inclusions were suitable for microthermometry measurement. Based on 16 primary fluid inclusions, those of aqueous inclusion assemblage undergo homogenization to the liquid phase (LAQ + V \rightarrow LAQ) between 120 and 140 °C. Based on the average $T_m(\text{Ice})$ value of -2.5 °C, the calculated salinity of the AQ inclusions is ca. 3.3 mass% in NaCl equivalent [using Bodnar's (1993) method].

Simultaneously with the complex vein system, a well-developed microstylolite system formed with an anastomosing geometry. The maximum amplitude is ~ 1 mm, and pressure solution films are easily detected on the CL images through their bright orange luminescent color.

Phase analysis (XRD, scanning, and Raman). The analyzed rock types consist of calcite crystals; other carbonate minerals (dolomite and aragonite) were not detected by the applied techniques.

The most common non-carbonate mineral is pyrite. It has a framboidal form and a bimodal size distribution and fabric position. The smaller sized crystals are related to biogenic components, while the larger ones appear in fractures. The mineral composition of the insoluble residue of the rock is summarized in Table 2. The results of the

Table 2
Average mineral composition of the studied rock types

	Type A limestone ^a	Type B limestone ^a	Dolomitic limestone ^b	Breccia ^a
Dolomite	–	–	37%	–
Quartz	–	–	–	<1%
Illite + muscovite	~20%	~60%–70%	–	~50%–60%
Pyrite	~30%	–	–	<1%
Dickite	~30%	~30%	–	~5%–10%
Anatase	~10%	–	–	~5%–10%
Gypsum	–	–	–	~5%–10%

^aValid for the insoluble residue

^bValid for the clay fraction of the insoluble residue

Table 3
 Calculated T_{\max} temperatures based on the carbonaceous material (on 18 samples) by Raman spectra

	Min	Max	Average	STD
Rahl et al. (2005)	192 °C	265 °C	226 °C	20
Lahfid et al. (2010)	210 °C	261 °C	233 °C	11.09
Beyssac et al. (2002)	333 °C	382 °C	348 °C	13.78
Zhou et al. (2014)	522 °C	599 °C	556 °C	23.04

thermometry calculations from the carbonaceous material uniformly suggest $T_{\max} \sim 220$ °C. The data are summarized in Table 3.

Mineral chemistry. The chemical analysis of the different cement phases by SEM-EDAX does not indicate high Mg calcite (>4 mol%). In addition, based on this measurement, there is no detectable difference in the composition of the two different-sized pyrite populations; both have a negligible amount of trace metals and can be regarded as pure FeS₂.

Based on the stable isotopic measurements, the carbon and oxygen isotopic composition of the host rock is $\delta^{18}\text{O}$: -4.0 (‰, V-PDB) and $\delta^{13}\text{C}$: +4 (‰, V-PDB) ($\pm 0.2\%$).

Limestone Type B

There is no significant difference between the Type A and Type B limestone regarding their framework composition; Type B limestone is also a peloidal and oncoidal grainstone. There are also no differences in their cement phases.

Based on the results of phase analysis, Type B is similar to Type A. The former is composed of pure calcite crystals; there is no trace of dolomite or aragonite. The amount of the dissolution residue is less than 1 m/m%. A significant difference from Type A appears regarding the mineral composition of the insoluble residue (summarized in Table 2); the dickite content of the residue is ~90%, which is much higher than the ~40% in Type A (Table 2).

Dolomitic limestone

Texture. The allochems are similar to those of the non-dolomitic limestone, suggesting a similar grainstone precursor texture. As a result of the fabric-selective dolomitization, a planar-E dolomite (Sibley and Gregg 1987) was developed (Fig. 5B).

Cement phases. The primary cement phases in the intergranular space are not recognizable due to the effect of dolomitization, but the abundance of the above-mentioned radial calcite cement is much higher than in the case of the

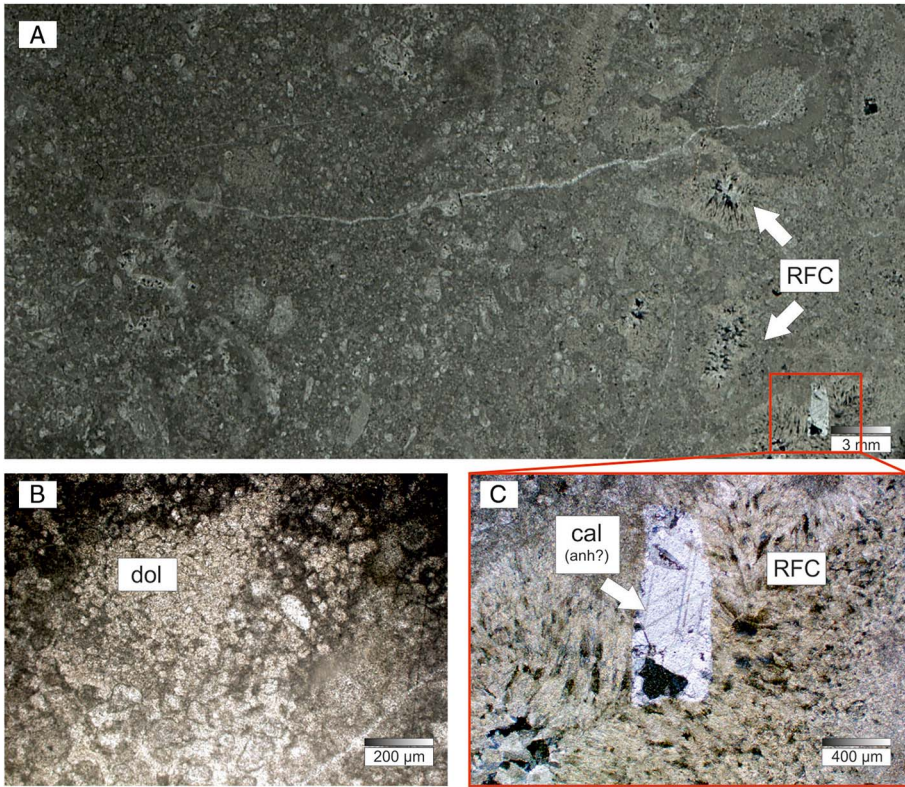


Fig. 5
Microphotos of the dolomitic limestone samples. A: Fabric of the rock type and the non-fabric-selective dolomitization. B: Euhedral dolomite crystals. C: Possible calcite pseudomorphs formed after anhydrite. (All microphotos taken in polarized light)

non-dolomitic limestone members. In several parts of the samples, large (>300 μm) calcite can be present. The shapes of the grains suggest that these calcite pseudomorphs formed after anhydrite crystals, but there is no measurement to prove this (Fig. 5C).

Breccia

Texture. Breccia zones are encountered mainly in the upper few meters of the Triassic carbonates, close to the proposed Triassic/Eocene boundary. Subordinately, breccia horizons are detected within the carbonate bodies in deeper zones as well. Based on the observations, the breccia at different horizons is rather similar, so their descriptions are summarized.

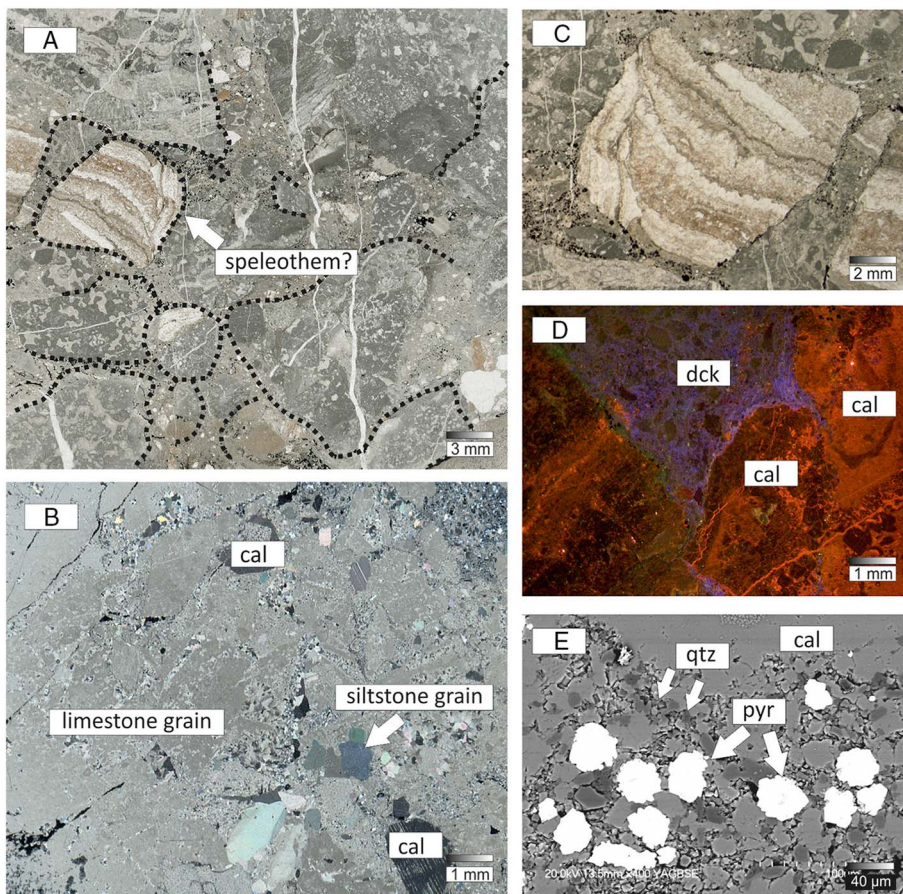


Fig. 6
 Photomicrographs of a breccia sample. A: Fabric of the breccia from the Triassic–Eocene boundary. B: Fabric of the breccia from the deeper part of the limestone. C: Laminated calcrete. D: CL image from the matrix. E: Framboidal pyrites from the matrix; dotted line shows the common presence of pyrites. (“A” and “C” microphotos taken with planar light; “B” taken in polarized light; “E” is a backscattered electron image)

The studied breccia occurrences have a polymictic composition (Fig. 6). Lithologically, the most common clast type is the limestone characterized above. Subordinate-ly, laminated calcrete clasts and those common in the overlying Eocene sequence (i.e., metamorphic rocks and siltstone) occur.

The average grain size of the different clast types is different. The limestone clasts are larger (centimeter scale), while the others are smaller than a few millimeters in diameter. The roundness for both the carbonate and non-carbonate clasts follows a normal distribution based on the Kolmogorov–Smirnov test, but the roundness of the majority of the carbonate grains is smaller than that of the non-carbonate grains

Table 4
Results of the image analysis. All parameters measured on 332 grains

	Min	Max	Average	STD
Area (mm ²)	0.04	92	5.96	14.16
Rotation	1.5	175	92	43
Roundness	0.21	0.97	0.63	0.17
Roughness	1.04	1.14	1.08	0.02
PSD = $-1.0072x + 9.3316$ ($R^2 = 0.9437$)				

(Table 4; Fig. 7). The variation coefficient of the main axis of the clasts (0.69) shows a chaotic texture. The packing density of the clasts is very variegated; grain-to-grain contacts are typical, but in some cases, there is more than a centimeter of space between the floating grains. The matrix content of the breccia layers is significant (>60%). Based on all these descriptive and numerical textural parameters, the breccia in question can be characterized as chaotic breccia (Mort and Woodcock 2008). The results of the image analysis are summarized in Fig. 7.

Matrix and cement phases. The matrix mostly consists of carbonate rock clasts and quartz, but calcite, anatase, feldspar, and muscovite mineral fragments are present as well.

Two different types of cement phases are defined by CL microscopy. There is a fine crystalline phase in the matrix with a bright purple luminescent color. Around the purple phase, there are numerous individual calcite crystals with dull orange luminescent color and a very bright orange overgrowth (Fig. 8). Based on the SE images, the purple phase seems to be a type of kandite mineral, which seems to be authigenic based on the SEM observations.

Microstructure. Only the F1 and F4 fracture generations are detectable in the breccia zones, whereas F2 and F3, which contain a large amount of bitumen, do not seem to be evolved in this lithology. The F1 generation is only detectable inside the carbonate clasts, while the F4 generation cuts the entire matrix. F4 fractures exhibit chaotic spatial distribution; they follow the surfaces of the larger clasts. Both microfracture generations (F1 and F4) have a notable secondary porosity by dissolution.

Microstylolite systems have not developed in the breccia zones, but the pressure solution is significant along the clast boundaries resulting in a stylobreccia texture.

Phase analysis. Based on the XRD measurements, the most common minerals in the matrix of the breccia are dickite (40%–50%), illite ± muscovite (25%–35%), and quartz (20%). Subordinately, pyrite, anatase, and goethite are detected as accessories.

Mineral chemistry. Three XRF maps were recorded from different regions of the matrix for the following elements: Si, Al, Fe, Mn, P, S, Ni, Co, Ba, Sr, Ce, and Pb. Based on the element maps, none of these elements show fabric-selective distribution.

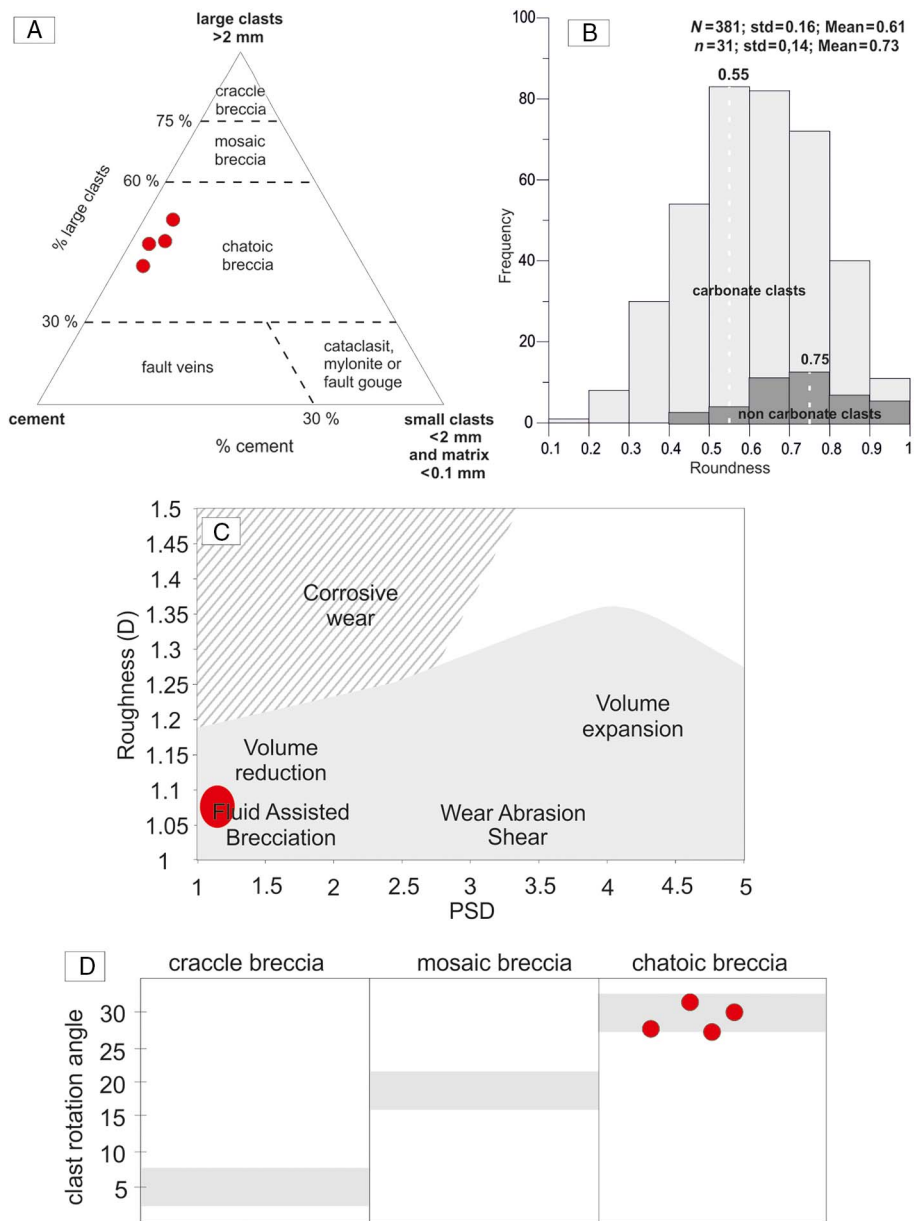


Fig. 7 Results of PIA. A and D: Classification by Mort and Woodcock (2008) diagrams. B: Distribution of roundness parameter by rock type categories. C: Potential generating processes (Jébrak 1997)

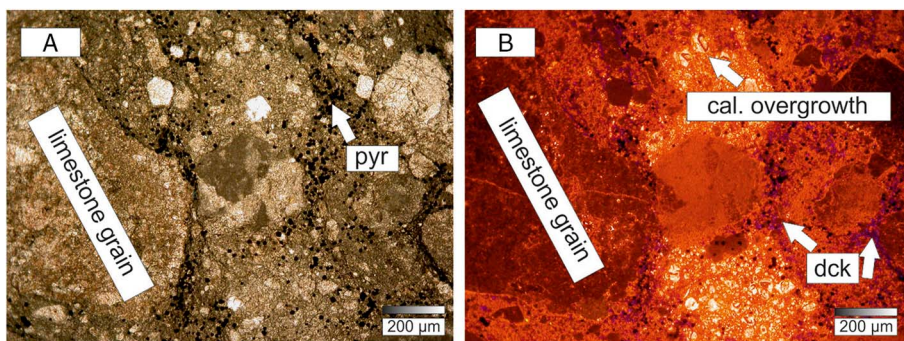


Fig. 8
Different calcite cement phases or overgrowth of the breccia on optical microphoto and on CL images. (All microphotos taken in planar light)

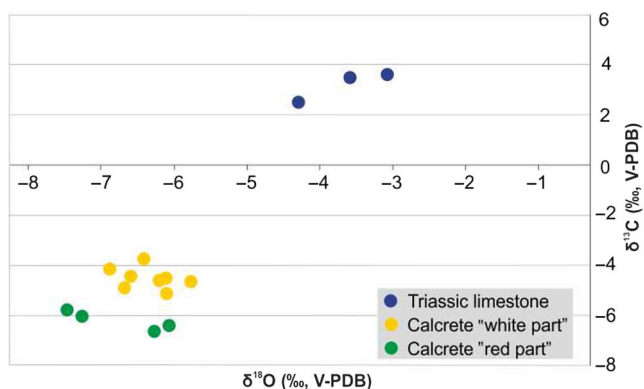


Fig. 9
Isotopic composition of the measured samples

The isotopic composition of a calcrete pebble is $\delta^{18}\text{O}$: ~ -6.5 (‰, V-PDB) and $\delta^{13}\text{C}$: ~ -6.0 (‰, V-PDB), while that for the limestone is $\delta^{18}\text{O}$: ~ -3.5 (‰, V-PDB) and $\delta^{13}\text{C}$: ~ 2.0 (‰, V-PDB) (± 0.2 ‰) (Fig. 9).

Discussion – Petrological characteristics of the main rock types

Limestone

Based on the core analysis, there are three different carbonate rock types in the reservoir. Among them, the most widespread is Type A limestone, which is an

oncoidal and peloidal grainstone. Due to the small amount of core samples, the exact classification of the rock types into lithostratigraphic units is very uncertain. Based on the geographical position of the investigated formations, the study area should belong to the Mid-Hungarian Mega-Unit, but a previous report (Benedek 2009) and data from the neighboring fields suggest that it is more likely a part of the Triassic Kisfennsík Limestone Formation or the Berva Limestone Formation in the Bükk Unit. As our results do not give any clear evidence to the contrary, the carbonate rocks in the studied reservoir are considered as a Bükk-type limestone, similar to the available MOL Report (Benedek 2009).

Tidal flat, lagoonal, and reefal environments have been reconstructed for the Kisfennsík Limestone in the Bükk Mountains (Velledits et al. 1999). The beds in the Gomba Field represent a different zone of the platform. The high energy part of the platform is represented by the well-sorted oncoidal samples (G-1 well) and the tidal flat is represented by the algal mat and the fenestral porosity of the samples (G-3 well). The stable isotopic data show a typical Triassic carbonate platform environment (Schimpf et al. 2011).

The mineralogical compositions of the limestone samples are relatively homogeneous; the studied core sections are composed of pure calcite. The proportions of non-carbonate phases are usually less than 1%. Quartz, pyrite, layer silicate phases (illite ± muscovite, dickite), anatase, and goethite appear as accessory minerals.

The finely dispersed distribution of euhedral crystals in the limestone is usually not an uncommon phenomenon; quartz often appears in such a textural position in hypersaline environments. Quartz with the observed morphological and mineralogical characteristics may crystallize during pedogenesis, or very shallow diagenesis (Nash et al. 2004; Varga and Raucsik 2014). Based on the geologic evolution of the study area (assuming an identical history to that of the Kisfennsík Limestone), pedogenesis could have affected the sediments during the Paleocene. Other substantiating signs of pedogenesis are not observed, which may have been the result of erosion.

The bimodal size distribution of the framboidal pyrites suggests two generations, but this observation is not definitely confirmed by their similar chemical compositions. Smaller pyrite grains (<15 µm) occur near the bioclasts or near the early cement phases; therefore, its formation is considered to be early diagenetic. A possible process that produced the pyrite may be sulfate reduction. In this case, the SO₄ content of the pore water is reduced by bacteria in the OM-rich environment, which leads to framboidal pyrite formation in the vicinity of concentrations of OM. The larger pyrite grains (>50 µm) occur detectably near the fracture system in both the Triassic carbonates and the Eocene breccia. Based on the experiments of Hallbach et al. (1993) and field observations of Sweeney and Kaplan (1973), framboidal pyrites may evolve under temperature conditions up to ~200 °C, while their minimum growth temperature under laboratory conditions without involving sulfate-reducing bacteria (SRB) is in the range of 65–80 °C. This temperature may even be 40–60 °C less than that needed under natural conditions (Maclean et al. 2008). In our case, there is no direct evidence for SRB contribution toward the generation of the larger pyrite crystals. However,

based on the OM Raman measurements (Table 3), our samples reached a higher temperature than the maximum possible formation temperature for framboidal pyrites, which can be explained by their textural position. In this case, the reduced material should not be the synsedimentary OM of the limestone; rather, it is the bitumen seal of the veins. Because OM in this position is likely a result of hydrocarbon migration, it is suggested that the carbonaceous material records the maximum temperature reached during burial, and the large pyrite crystals grew in the course of the uplift following oil migration to the reservoir.

There are several subsequent cement phases in the analyzed samples. The prismatic, radial, and limpid calcite cement, enveloping the ooids and oncoids, is considered to be the first phase (Fig. 3B). It has low Mg content (<4 mol%), which may suggest a meteoric origin (Hayes and Boles 1993). Based on its textural position, this phreatic cement possibly formed during early (shallow) diagenesis close to the surface.

RFC, which can form in different environments, is clearly in younger textural position than the above-mentioned phreatic cement. New research (Richter et al. 2011) indicates that it could develop not only in marine phreatic zones but also in a continental vadose zone, and the resulting cement may form by both diverse biogenic and abiogenic processes. Although the most common environment of this cement type is the intertidal and upper bathyal zone up to 600 m depth (Richter et al. 2011), this cement also has been documented to form in numerous caves (Neuser and Richter 2007; Richter et al. 2011). The position of the RFCs in the samples is not fabric selective. Based on its low Mg/Ca ratio, this calcite may also have precipitated from meteoric fluids, which is in good agreement with the results of Wilson and Dickson (1996), who said that RFC forms from meteoric fluids instead of seawater in subtropical or tropical platforms. Based on its texture, mineral chemistry and worldwide analogs, the RFC in our samples is interpreted as early diagenetic cement.

The Mg/Ca ratio of the BC cement is low, and the crystals enclose numerous tiny dolomite inclusions, which are typically only a few micrometers across. The presence of dickite in the limestone shows a burial formation temperature as high as >200 °C (Zotov et al. 1998). This value is consistent with the calculated maximum temperature based on the typical Raman spectra of the carbonaceous material ($\sim 220 \pm 50$ °C).

The tectonic evolution of the region had to be rather complex as suggested by the subsequent brittle deformation events recorded by fractures and intense brecciation. The real age of the vein filling by calcite is unknown, but the microstructural results show that the F1–F3 fracture generations are older than the main brecciation event, while the last generation (F4) must be earlier than the process that formed the breccia structure. Furthermore, we know that the vein filling in F3 has bitumen with high T_{\max} , while the F4 generation calcite contains fluid phase hydrocarbon inclusions. All the data indicate that the above-mentioned uplift happened after the cementation of the F3 fractures but prior to or during the F4 filling by calcite, when the formation temperature was lower than in the case of F3 (Fig. 10). This model is supported by the microthermometry of the F4 generation fluid inclusions (based on 16 samples)

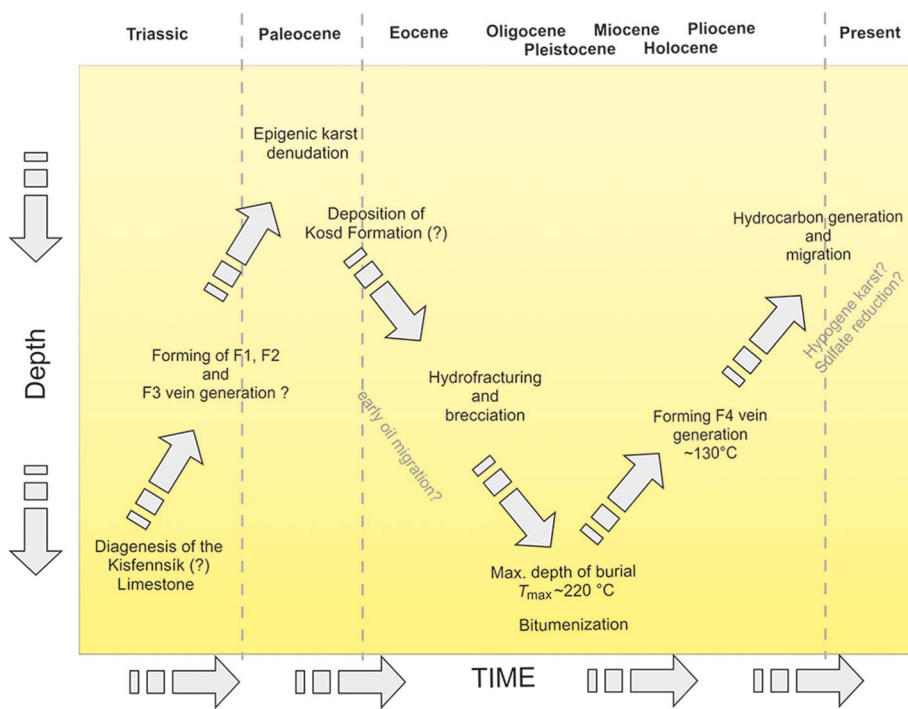


Fig. 10
Schematic depth–time diagram of the observed diagenetic events

(Fig. 11A). The primary fluid inclusions show a ~ 125 °C homogenization temperature, which is similar to the temperature of the recent pore fluid. The data suggest that the F4 fracture generation formed due to relaxation during the uplift phase. This fracture generation has to be a part of the presently active reservoir as supported by the similarity of the spectra of the oil inclusions and the produced crude oil (Fig. 11B).

Dolomitic limestone

Limestone with dolomite content of $>40\%$ is defined as dolomitic limestone in this study using Chilingar's terminology (1960). The original packstone texture of the rock type is recognizable in all the studied samples despite the destructive dolomitization. This texture is interpreted as a low-energy sedimentation environment, most likely along the back reef lagoon of a carbonate platform. We interpreted the calcite pseudomorphs, implying an intensive evaporation process. Dolomitic limestone samples came from the bottom depth of 2,680 m, from the very bottom of the Gomba-1 well. Continuity of the facies below this depth is not known; nevertheless, it may be a more significant part of the reservoir than was previously believed.

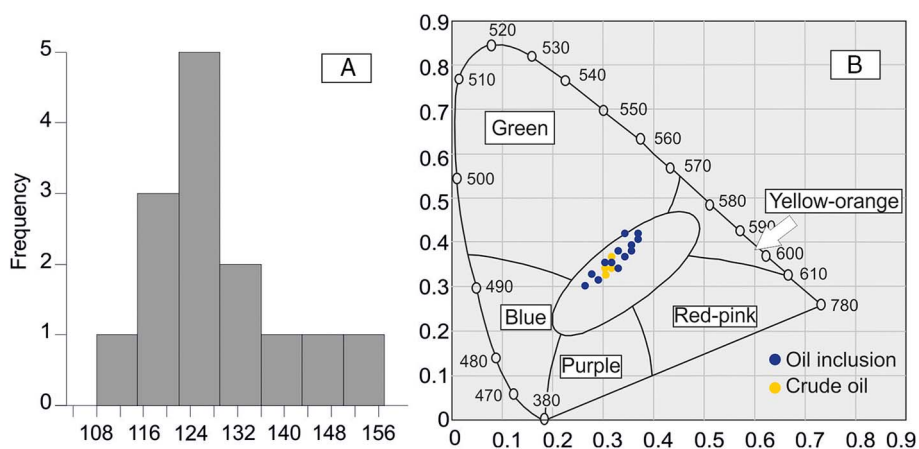


Fig. 11 Results of the microthermometry and the UV spectroscopy on the fluid and oil inclusions. A: Homogenization temperature of the primary water content fluid inclusions (light gray) and the T_{\max} distribution of the Raman measurements on the bitumen in the F3 vein generation (dark gray). B: Similarity of the UV spectra of the crude oil and the oil inclusions

Breccia

Based on the study results, breccia occurs in two different stratigraphic positions in the reservoir (Fig. 1). The thicker horizon is located at the Triassic–Eocene unconformity, while the thinner zones are observed below the unconformity, inside the carbonate body surrounded by homogeneous limestone beds that were significantly altered by deformation events (both brittle and ductile deformation).

The investigated breccia types are rather heterogeneous, both concerning composition and structure. The most common and largest clasts consist of the above-described carbonates, but there are also metamorphic and siltstone fragments. Based on the results of isotopic measurements on the calcrite-like fragments, the parent fluid of this fragment was of meteoric origin. Consequently, these fragments cannot be stromatolite fragments, but these clasts may represent pieces of calcite veins or any fresh-water limestone form, e.g., a speleothem or a laminated accrete fragment. As there is no data in the literature about a vein type similar to these fragments from the wider region, the laminated carbonate clasts are considered to be speleothems (e.g., dripstone fragments). This seems to be supported by the measured isotope values; McDermott et al. (2001) and Verheyden et al. (2008) measured similar values in speleothems.

The subordinate mineral grains in the matrix (quartz, anatase, feldspar, and dickite) of the breccia are not typical in the limestone described above. The CL color of the kaolinite group mineral in the matrix (purple) is problematic. Based on Boggs and Krinsley (2008) and Götze et al. (2002), the color of the kaolinite and dickite is deep

blue instead of the experienced purple. The most likely reason is that the CL spectrum is shifted due to irradiation by an intensive electron beam (Götze et al. 2002). The mass proportion of the dissolution residue of the breccia is ~ 10 m/m%, i.e., 10 times what is typical for the carbonate samples. The most probable reason for the relative increase in the insoluble residue is the decreasing carbonate content caused by dissolution. Nevertheless, in the case of dissolution, the clasts should show a very complicated shape (Jébrak 1997), which has not been observed in the present case. That is why the occurrence of these mineral grains should be the result of postdiagenetic brecciation rather than syngenetic, intrabasinal transportation.

The basal member of the Kosd Formation in the Bükk Unit consists of 2–25-cm-sized gravel, which mainly represents the Kiszfennsík Limestone (Less 2005). The breccia studied in the Gomba wells is identical to the Kosd Formation described by Benedek (2009), even if the roundness of the clasts from the Kosd Formation usually increases to the SW (toward the Gomba Field) (Less 2005), which is not typical here at all. In this study, this formation is called the BPC. The roundness of the carbonate clasts in the BPC is smaller on average (0.63) than that for non-carbonate clasts (0.73) (Fig. 7B), which suggests that the more resistant non-carbonate clasts represent a longer distance transport and thus a more distant source area, while the carbonate clasts were derived from a much more proximal source; most likely they did not move at all. This latter model is coherent with the presence of the well-preserved supposed speleothems in the breccia because speleothems cannot withstand transportation. In addition, the unimodal, normal distribution of the roundness data of the carbonate clasts suggests that there was only a single process responsible for their shape.

Possible interpretations of the breccia formation

Breccia-texture rocks can be formed by tectonic processes (compression or extension stress field) or can be formed by syngenetic processes as well (e.g., regolith or other sediments). In our case, we try to define those processes that can describe the breccia formation in two different depths.

Hydrobreccia – Cave sediment theory

Using the classification scheme of Jébrak (1997), the breccia zones in the Gomba Field could be interpreted as hydraulic breccia based on their measured geometric parameters (Fig. 7C). Similar rocks are known from the wider surroundings at the Triassic–Eocene boundary (Magyari 1994), confirming that the genetics of the breccia in this study may be similar to those widespread around the karstic area in the Buda Mountains. This locality is as close as 50 km to the west of the Gomba Field. Here, based on the model of Magyari (1994), marls with high fluid content were deposited and infiltrated into the surface of the fractured and karstified Triassic limestone in the

early Eocene. Brecciation in the Buda Hills was due to the collapse of the steep marginal cliffs of the abrasional coastline (coincident with a synsedimentary fault scarp). It is supposed that the collapse was triggered by earthquakes and the sudden deposition of the voluminous rock fall episodically increased the pore pressure to such an extent as to result in hydrofracturing and further brecciation. These breccia occurrences have very similar textural features to those described in the Gomba wells; both are matrix supported, there are no shear indicators in the matrix or along the rock fragments and the roundness of the grains varies.

In our concept, fluvial sediments (Kosd Formation?) with high fluid content were deposited onto the karstified surface and subsided into greater depths afterward. Because of the impermeable cover (marly and clayey sequences), the fluids infiltrated into the volumes of primary, secondary and tertiary porosity were unable to escape through the existing microfracture system; the fluids must have caused overpressure and brecciation through hydrofracturing during the Oligocene or later (Fig. 10).

In addition to the geometric parameters of the clasts (Fig. 7), the textural position of the pyrite coating on the rock fragments supports this theory. The youngest fingerprints of the evolution preserved in the samples are the above-mentioned larger pyrites along the F4 vein generation. The maximum formation temperature of the framboidal pyrites is approximately 200 °C. As the temperature of the maximum burial in the study area was $\sim 220 \pm 50$ °C (based on the Raman measurements), this pyrite generation had to crystallize during an uplift event; however, the circumstances of this event are not known. At present, the temperature of the warmest fluids in the carbonate reservoir is ~ 130 °C, much lower than the T_{\max} value measured on the carbonaceous material. Geochemical analyses had previously confirmed that hydrocarbons are still migrating from the Triassic layers toward the Eocene conglomerates, which are also rich in pyrite (Benedek 2009). The pyrite in the BPC (Kosd Formation?) has an identical textural position to that in the Triassic carbonate breccia where it coats the clasts. The similarities between these pyrites suggest that the pyrite formed according to the same process. According to our hypothesis, the framboidal pyrite zone formed at the front of the migrating hydrocarbons. In the deep zones, where the temperature was above 100–160 °C, hydrocarbons could produce H₂S-rich fluids by thermal sulfate reduction (Machel 2001). When these fluids reached the actual (130 °C) (or lower) temperature, framboidal pyrites formed near the migration pathways. Framboidal pyrites are usually the sign of bacterial sulfate reduction which is normally active only up to 60–80 °C (Machel 2001), but framboidal pyrites can form by the replacement of greigite with pyrite in hydrothermal environment as well. In this case, there is not enough information about the pyrites to reconstruct the forming mechanism. Hydrogen sulfide that developed by sulfate reduction could have increased the pore volume, as is observable in the cores (Fig. 3A).

Hydrofracturing as a model can give an adequate interpretation for the genetics and evolution of the breccia at the Triassic–Eocene boundary but cannot explain the polymictic breccia in the deeper parts of the carbonate body. Following the

nomenclature of Loucks (1999), these rocks can be classified as “matrix supported chaotic breccias.” Based on recent analogies, the formation of this breccia type is possible either by cave wall collapse or fluvial transportation (White and White 1969). Both processes inevitably require a well-developed karst. Well-developed karst aquifers have a relatively large storage capacity but water flows through the system unobstructed in conduits at high velocity (up to $\text{m/h} \cdot 10^2$) (Stevanović 2015). This high flow velocity is necessary for the transportation of the coarse sediments. Based on the analogies from the Transdanubian Mega Unit and the Bükk Unit, there was intensive epigenetic karstification during the Paleocene and early Eocene, which resulted in a dissected surface. Based on these analogies, it is presumable that the buried Gomba reservoir was karstified, at least during the Paleocene and early Eocene, because it was in an uplifted position and there was significant precipitation during these times (Bowen et al. 2005). Due to the small amount of breccia samples from the deeper section, it is impossible to recognize their genetics, but this rock type can be an indirect evidence of karst processes. Based on its stratigraphic position and petrographic and microstructural features, it can be suggested that the breccia in the deeper section possibly represents collapse breccia and, in part, cave sediments.

Regolith theory

As an alternative of the hydrobreccia model, another one introduced by Nádor (1991, 1993) can be applied as well. Nádor (1993) investigated the paleokarst of the Buda Mountains, where numerous breccia outcrops occur along the Triassic–Eocene boundary. This breccia is interpreted as a regolith that formed by tectonic events, when the area was uplifted, possibly resulting in erosion of Jurassic and Cretaceous pelagic sediments during this long subaerial period. As a consequence, the underlying Triassic carbonates became exposed to meteoric waters (Nádor 1993). Due to tropical climatic conditions, Late Cretaceous and early Eocene weathering may have resulted in kaolinite formation instead of dickite. The kaolinite/dickite alteration is a very common process both in diagenetic environment and hydrothermal environment. Based on Ehrenberg et al. (1993) and Beaufort et al. (1998), the alteration works at 120–130 °C, while Choo and Kim (2004) suggest higher temperatures, namely, 250–290 °C. Ehrenberg et al. (1993) says that kaolinite/dickite conversion is inhibited by the invasion of the hydrocarbons. This is in accordance with our results which show that breccia formation was preceded by the hydrocarbon migration.

While the regolith theory can in part describe the breccia formation at the Triassic–Eocene boundary, it cannot explain the evolution of the deeper breccia zones at all. Most probably, they form a collapse breccia and, in part, also cave sediment as detailed above.

Although there is not enough information to distinguish between the two possible scenarios concerning the breccia formation at the Triassic–Eocene boundary, mineralogical and rock fabric data suggest that the hydrobreccia concept is the most plausible explanation for the observed brecciated horizons.

Conclusions

The analyzed cores suggest a complex history of the reservoir, especially concerning its karstic and structural evolution. Karstification is supposed to have been responsible for the development of the several meters thick, high permeability zone at the Triassic–Eocene boundary, which, from a genetic point of view, can be either a hydraulically fractured breccia zone or a regolith. The polymictic breccia horizons in the deeper zones can be interpreted as paleocave facies, collapse, and/or cave sediments. While the upper breccias, independent of their genetics, represent a laterally extensive blanket-like formation, relics of the hypothetical cave are probably of linear geometry. This kind of difference may have a peculiar effect on the internal structure, and thus on the hydrodynamics, of the whole karstic reservoir. From this perspective, the role of the F4 fracture generation seems essential as well. Hydrocarbon fluid inclusions in the vein-cementing calcite and the crude oil produced in the area are of identical composition suggesting that the F4 structure must be a part of the recent fluid migration pathway. To better understand the behavior of the rather complex fractured Gomba reservoir, interconnection between the two breccia horizons and the F4 fracture network should be modeled.

Acknowledgements

The authors would like to thank MOL Plc for providing the core material, thin sections, and reports that were essential for this research, as well as the Institute for Geological and Geochemical Research of Hungary for the cathodoluminescence and stable isotope measurements.

References

- Árkai, P. 1983: Very low- and low grade alpine regional metamorphism of the Paleozoic and Mesozoic formations of The Bükkium, NE-Hungary. – *Acta Geologica Hungarica*, 26/1–2, pp. 83–101.
- Beaufort, D., A. Cassagnabere, S. Petit, B. Lanson, G. Berger, J.C. Lachapagne, H. Johansen 1998: Kaolinite-to-dickite reaction in sandstone reservoirs. – *Clay Minerals*, 33, pp. 297–316.
- Benedek, L. 2009: Gomba mező geológiai újrafeldolgozása és művelési terve (Operation plan and reprocessing of the Gomba field). – MOL Plc. Report, Budapest, 210 p. (in Hungarian)
- Beyssac, O., B. Goffé, C. Chopin, J.N. Rouzaud 2002: Raman spectra of carbonaceous material in metasediments: A new geothermometer. – *Journal of Metamorphic Geology*, 20, pp. 859–871.
- Blenkinsop, T.G. 1991: Cataclasis and processes of particle size reduction. – *Pure and Applied Geophysics*, 136, pp. 1–33.
- Bodnar, R.J. 1993: Revised equation and table for determining the freezing point depression of H₂O–NaCl solutions. – *Geochimica et Cosmochimica Acta*, 57, pp. 683–684.
- Boggs, S., D. Krinsley 2008: Application of Cathodoluminescence Imaging to the Study of Sedimentary Rocks. – Cambridge University Press, Cambridge, USA, 165 p.

- Bons, P.D., M.A. Elburg, E. Gomez-Rivas 2012: A review of the formation of tectonic veins and their microstructures. – *Journal of Structural Geology*, 43, pp. 33–62.
- Bowen, G.J., L.I. Wassenaar, K.A. Hobson 2005: Global application of stable hydrogen and oxygen isotopes to wildlife forensics. – *Oecologia*, 143, pp. 337–348.
- Candelaria, M.P., C.L. Reed (Eds) 1992: Paleokarst, Karst Related Diagenesis and Reservoir Development: Examples from Ordovician–Devonian Age Strata of West Texas and the Mid-Continent. – Permian Basin Section SEPM Publication, 92–33, 202 p.
- Chilingar, G.V. 1960: Notes on classification of carbonate rocks on basis of chemical composition. – *Journal of Sedimentary Petrology*, 30, pp. 157–158.
- Choo, O.C., S.J. Kim 2004: Dickite and other kaolin polymorphs from an Al-rich clay deposits formed in volcanic tuff, southeastern Korea. – *Clays & Clay Minerals*, 52, pp. 749–759.
- Coplen, T.B. 1996: Guidelines for reporting certain isotopic values relevant to ground-water studies. – *Ground Water*, 34/3, p. 388.
- Csontos, L., A. Nagymarosy 1998: The Mid-Hungarian line: A zone of repeated tectonic inversions. – *Tectonophysics*, 297/1–4, pp. 51–71.
- Dolton, G.L. 2006: Pannonian Basin Province, Central Europe (Province 4808) – Petroleum geology, total petroleum systems, and petroleum resource assessment. – U.S. Geological Survey Bulletin, 2204/B, p. 47.
- Dunham, R.J. 1962: Classification of carbonate rocks according to depositional texture. – AAPG Memoir, 1, pp. 108–121.
- Ehrenberg, S.N., P. Aagard, M.J. Wilson, A.R. Fraser, D.M.L. Duthie 1993: Depth-dependent transformation of kaolinite to dickite in sandstones of the Norwegian continental shelf. – *Clay Minerals*, 28, pp. 325–352.
- Esteban, M., T. Budai, E. Juhász, P. Lapointe 2009: Alteration of Triassic carbonates in the Budai Mountains – A hydrothermal model. – *Central European Geology*, 52/1, pp. 1–29.
- Flook, A.G. 1978: Use of dilation logic on the Quantimet to achieve fractal dimension characterization of texture and structured profiles. – *Powder Technology*, 21, pp. 295–298.
- Fritz, R.D., J.L. Wilson, D.A. Yurewicz 1993: Paleokarst Related Hydrocarbon Reservoirs. – SEPM Core Workshop, Tulsa, OK, USA, 18, 275 p.
- Goldstein, R.H., T.J. Reynolds 1994: Systematics of Fluid Inclusions in Diagenetic Minerals. – SEPM Short Course, Tulsa, OK, USA, 31, 203 p.
- Götze, J., M. Plötze, T. Götte, R.D. Neuser, D.K. Richter 2002: Cathodoluminescence (CL) and electron paramagnetic resonance (EPR) studies of clay minerals. – *Mineralogy and Petrology*, 76, pp. 195–212.
- Győri, O., Z. Poros, A. Mindszenty, F. Molnár, L. Fodor, R. Szabó 2011: Budai-hegységi paleogén karbonátos kőzetek diagenézistörténete (Diagenetic history of the Paleogene carbonates, Buda Hills, Hungary). – *Földtani Közlöny*, 141/4, pp. 341–361. (in Hungarian)
- Haas, J. (Ed) 2004: Magyarország Geológiája. Triász (Geology of Hungary. Triassic). – Eötvös Kiadó, Budapest, Hungary, 306 p. (in Hungarian)
- Haas, J., T. Budai, L. Csontos, L. Fodor, Gy. Konrád 2010: Pre-Cenozoic Geological Map of Hungary, 1:500 000. – Geological and Institute of Hungary, Budapest.
- Halbach, P., B. Pracejus, A. Marten 1993: Geology and mineralogy of massive sulfide ores from the central Okinawa trough, Japan. – *Economic Geology*, 88/8, pp. 2210–2225.
- Hayes, M.J., J.R. Boles 1993: Evidence for meteoric recharge in the San Joaquin Basin, California provided by isotope and trace element chemistry of calcite. – *Marine and Petroleum Geology*, 10, pp. 135–144.
- Jébrak, M. 1997: Hydrothermal breccias in vein-type ore deposits: A review of mechanisms morphology and size distribution. – *Ore Geology Reviews*, 12, pp. 111–134.
- Kecskeméti, T. 1998: Magyarország epikontinentális eocén képződményeinek rétegtana (Stratigraphy of the epicontinental Eocene formations of Hungary). – In: Bérczi, I., Á. Jámor (Eds): Magyarország Geológiai Képződményeinek Rétegtana (Stratigraphy of the Hungarian Geological Formations). MOL Plc. and Geological and Institute of Hungary, Budapest, Hungary, pp. 403–417. (in Hungarian)

- Kókai, J., Gy. Pogácsás 1991: Tectono-stratigraphical evolution and hydrocarbon habitat of the Pannonian Basin. – In: Spencer, A.M. (Ed): Generation, Accumulation and Production of Europe's Hydrocarbons. Special Publication of the European Association of Petroleum Geoscientists, Berlin, Germany, 1, p. 307–317.
- Korpás, L., E. Juhász 1990: Paleokarszt földtani modellek (Paleokarst geological models). – *Karszt és Barlang*, 2, pp. 105–116. (in Hungarian)
- Kovács, S., T. Szederkényi, J. Haas, Gy. Buda, G. Császár, A. Nagymarosy 2000: Tectonostratigraphic terranes in the pre-Neogene basement of the Hungarian part of the Pannonian area. – *Acta Geologica Hungarica*, 43/3, pp. 225–328.
- Kraus, S. 1982: A Budai-hegység hévizes barlangjainak fejlődéstörténete (Evolution of the hydrothermal caves in the Buda Mountains). – *Karszt és Barlang*, 1, pp. 29–34. (in Hungarian)
- Kriván, P. 1959: Mezozoós karsztosodási és karsztlefedési szakaszok, alsóbartoni sziklásparti jelenségek a Budai-hegységben. A szubgresszió fogalma (Phases de karstification et de karst couvert Mésozoïques, phénomènes de falaise du Bartonien inférieur dans la Montagne de Buda. La notion de subgression). – *Földtani Közlöny*, 89/4, pp. 393–401. (in Hungarian)
- Lahfid, A., O. Beysse, E. Deville, F. Negro, C. Chopin, B. Goffé 2010: Evolution of the Raman spectrum of carbonaceous material in low-grade metasediments of the Glarus Alps (Switzerland). – *Terra Nova*, 22/5, pp. 354–360.
- Less, Gy. 2005: Paleogene. – In: Pelikán, Gy. (Ed): Geology of the Bükk Mountains. Hungarian Geological Society, Budapest, Hungary, pp. 204–210.
- Loucks, R.G. 1999: Paleocave carbonate reservoirs: Origins, burial-depth modifications, spatial complexity, and reservoir implications. – *AAPG Bulletin*, 83/11, pp. 1795–1834.
- Loucks, R.G., P.K. Mescher, G.A. McMechan 2004: Three-dimensional architecture of a coalesced, collapsed-paleocave system in the Lower Ordovician Ellenburger Group, central Texas. – *AAPG Bulletin*, 88/5, pp. 545–564.
- Lucia, F.J. 1968: Sedimentation and paleogeography of the El Paso group. – In: Stewart, W.J. (Ed): Delaware Basin Exploration. West Texas Geological Society Guidebook, Midland, TX, USA, 68–55, pp. 61–75.
- Lucia, F.J. 1995: Lower Paleozoic cavern development, collapse, and dolomitization, Franklin Mountains, El Paso, Texas. – In: Budd, D.A., A.H. Saller, P.M. Harris (Eds): Unconformities and Porosity in Carbonate Strata. AAPG, Austin, TX, USA, 63, pp. 279–300.
- Lucia, F.J. 1996: Structural and fracture implications of Franklin Mountains collapse brecciation. – In: Stouder, E.L. (Ed): Precambrian–Devonian Geology of the Franklin Mountains, West Texas, Analogs for Exploration and Production in Ordovician and Silurian Karsted Reservoirs in the Permian Basin. WTGS Publication, Midland, TX, USA, 96–100, pp. 117–123.
- Lucia, F.J., C. Kerans, G.W. Vander Stoep 1992: Characterization of a karsted, high-energy, ramp-margin carbonate reservoir: Taylor-Link West San Andres Unit, Pecos County, Texas. – Report of Investigations, University of Texas at Austin, Bureau of Economic Geology, Budapest, Hungary, 208, 46 p.
- Machel, H.G. 2001: Bacterial and thermochemical sulfate reduction in diagenetic settings – Old and new insights. – *Sedimentary Geology*, 140, pp. 143–175.
- MacLean, L.C., T. Tylliszczak, P.U. Gilbert, D. Zhou, T.J. Pray, T.C. Onstott, G. Southam 2008: A high-resolution chemical and structural study of framboidal pyrite formed within a low-temperature bacterial biofilm. – *Geobiology*, 6/5, pp. 471–480.
- Magyari, Á. 1994: Késő-cocén hidraulikus breccsásodási jelenségek a Budai hegység déli részén (Late Eocene hydraulic brecciation in the Southern Buda Mountains, Hungary). – *Földtani Közlöny*, 124/1, pp. 89–107. (in Hungarian)
- McDermott, F., D.P. Matthey, C.J. Hawkesworth 2001: Centennial-scale Holocene climate variability revealed by a high-resolution speleothem $\delta^{18}\text{O}$ record from SW Ireland. – *Science*, 294, pp. 1328–1331.
- McKinney, C.R., J.M. McCrea, S. Epstein, H.A. Allen, H.C. Urey 1950: Improvements in mass spectrometers for the measurement of small differences in isotope abundance ratios. – *Review of Scientific Instruments*, 21, p. 724.

- Milliam, J.D. 1974: Marine Carbonates. Part 1: Recent Sedimentary Carbonates. – Springer-Verlag, New York, USA, 375 p.
- Mort, K., N.H. Woodcock 2008: Classification of fault breccias and related fault rocks. – *Geological Magazine*, 145/3, pp. 435–440.
- Nádor, A. 1991: A Budai-hegység paleokarsztjai és fejlődéstörténetük (Evolution of the paleokarsts in the Buda-Hills). – PhD dissertation, Eötvös Loránd University, Budapest, Hungary, 171 p. (in Hungarian)
- Nádor, A. 1993: Paleokarsts and long-term Karst evolution of the Buda Mountains, Hungary. – *Bulletin de la Société géologique de Liège*, 29, pp. 139–143.
- Nádor, A., L. Sásdi 1991: A Budai-hegység paleokarsztjai és fejlődéstörténetük. 1. rész: Termális hatást nem tükröző paleokarsztok (Evolution of the paleokarsts in the Buda-Hills. Part 1: Non-thermal paleokarsts). – *Karszt és Barlang*, 1–2, pp. 3–10. (in Hungarian)
- Nádor, A., L. Sásdi 1995: A Budai hegység termális paleokarsztjai (Thermal paleokarst of the Buda-Hills). – *Karszt és Barlangkutatás*, 10, pp. 17–23. (in Hungarian)
- Nagymarosy, A. 1990: Paleogeographical and paleotectonic outlines of some Intra Carpathian Paleogene basins. – *Geologica Carpathica*, 41/3, pp. 259–274.
- Nash, D.J., S.J. McLaren, J.A. Webb 2004: Petrology, geochemistry and environmental significance of silcrete-calcrete integrate duricrusts at Kang Pan and Tshwane, central Kalahari, Botswana. – *Earth Surface Processes and Landforms*, 29, pp. 1559–1586.
- Neuser, R.D., D.K. Richter 2007: Non-marine radiaxial fibrous calcites – Examples of speleothems proved by electron backscatter diffraction. – *Sedimentary Geology*, 194, pp. 149–154.
- Pelikán, Gy. 2005: Geology of the Bükk Mountains. – Hungarian Geological Society, Hungary, Budapest, 284 p.
- Poros, Zs., A. Mindszenty, F. Molnár, J. Pironon, O. Györi, P. Ronchi, Z. Szekeres 2012: Imprints of hydrocarbon-bearing basinal fluids on a karst system: Mineralogical and fluid inclusion studies from the Buda Hills, Hungary. – *International Journal of Earth Sciences*, 101, pp. 429–452.
- Rahl, J.M., K.M. Anderson, M.T. Brandon, C. Fassoulas 2005: Raman spectroscopic carbonaceous material thermometry of low grade metamorphic rocks: Calibration and application to tectonic exhumation in Crete, Greece. – *Earth and Planetary Science Letters*, 240, pp. 339–354.
- Richter, D.K., R.D. Neuser, J. Schreuer, H. Gies, A. Immenhauser 2011: Radiaxial-fibrous calcites: A new look at an old problem. – *Sedimentary Geology*, 239/1–2, pp. 23–36.
- Schimpf, D., R. Kilian, A. Kronz, K. Simon, C. Spötl, G. Wörner, A. Mangini 2011: The significance of chemical, isotopic, and detrital components in three coeval stalagmites from the superhumid southernmost Andes (53°S) as high-resolution palaeo-climate proxies. – *Quaternary Science Reviews*, 30/3–4, pp. 443–459.
- Schmid, S.M., D. Bernoulli, B. Fügenschuh, L. Matenco, S. Schefer, R. Schuster, K. Ustaszewski 2008: The Alpine-Carpathian-Dinaridic orogenic system: Correlation and evolution of tectonic units. – *Swiss Journal of Geosciences*, 101/1, pp. 139–183.
- Shepherd, T.J., A.H. Rankin, D.H.L. Alderton 1985: A Practical Guide to Fluid Inclusion Studies. – Blackie and Son Ltd., London, UK, 239 p.
- Sibley, D.F., J.M. Gregg 1987: Classification of dolomite rock textures. – *Journal of Sedimentary Petrology*, 57, pp. 967–975.
- Smith, T., J. Guild 1931: The C.I.E. colorimetric standards and their use. – *Transactions of the Optical Society*, 33/3, pp. 73–134.
- Spötl, C., T.W. Wennemann 2003: Continuous-flow isotope ratio mass spectrometric analysis of carbonate minerals. – *Rapid Communications in Mass Spectrometry*, 17, pp. 1004–1006.
- Stevanović, Z. 2015: Karst Aquifers – Characterization and Engineering. – Springer, 689 p.
- Sweeney, R.E., I.R. Kaplan 1973: Pyrite framboid formation: Laboratory synthesis and marine sediments. – *Economic Geology*, 68, pp. 618–634.
- Szalay, I., E. Dienes, I.L. Nemes, L. Schönviszky 1978: A Darnó-öv szerkezeti kutatása (Investigation of the Darnó-belt). – Annual Report of Eötvös Loránd Geophysical Institute, 1977, Budapest, Hungary, pp. 34–41. (in Hungarian)

- Szalay, I., K. Dudás, E. Hegedűs, L. Schönviszky, S. Taba 1976: Geophysical structure investigation around the Damó fault line. – Annual Report of Eötvös Loránd Geophysical Institute, 1975, Budapest, Hungary, pp. 26–30.
- Tari, G., T. Báldi, M. Báldi-Beke 1993: Paleogene retroarc flexural basin beneath the Neogene Pannonian Basin: A geodynamic model. – *Tectonophysics*, 226/1, pp. 433–455.
- Varga, A., B. Raucsik 2014: Pedogenic calcrete records in southern Transdanubia, Hungary: A brief review with paleoenvironmental and paleogeographic implications. – *Central European Geology*, 57/2, pp. 137–151.
- Velledits, F., A. Bérczi-Makk, O. Piros 1999: A Kiszécsényi Mészakő (Bükk hegység) fáciese és kora (Facies and age of the Kiszécsény Limestone, Bükk Mts.). – *Földtani Közlöny*, 129/4, pp. 573–592. (in Hungarian)
- Verheyden, S., D. Genty, O. Cattani, M. Vanbreukelen 2008: Water release patterns of heated speleothem calcite and hydrogen isotope composition of fluid inclusions. – *Chemical Geology*, 247/1–2, pp. 266–281.
- Wein, Gy. 1977: A Budai-hegység szerkezete (A Budai-hegység kialakulásának története) (Tectonics of the Buda Mountains). – *Földtani Közlöny*, 107/3–4, pp. 329–347. (in Hungarian)
- White, E.L., W.B. White 1969: Processes of cavern breakdown. – *National Speleological Society Bulletin*, 31, pp. 83–96.
- Wilson, P.A., J.A.D. Dickson 1996: Radial calcite: Alteration product of and petrographic proxy for magnesian calcite marine cement. – *Geology*, 24, pp. 945–948.
- Yui, T.F., E. Huang, J. Xu 1996: Raman spectrum of carbonaceous material: A possible metamorphic grade indicator for low-grade metamorphic rocks. – *Journal of Metamorphic Geology*, 14/4, pp. 115–124.
- Zhou, Q., X.M. Xiao, L. Pan, H. Tian 2014: The relationship between micro-Raman spectral parameters and reflectance of solid bitumen. – *International Journal of Coal Geology*, 121/1, pp. 19–25.
- Zotov, A., M. Galeev, J. Schott 1998: An experimental study of Kaolinite and Dickite Relative stability at 150–300 °C and the Thermodynamic properties of Dickite. – *American Mineralogist*, 83, pp. 516–524.